electronic reprint

STRUCTURAL BIOLOGY
COMMUNICATIONS

ISSN: 2053-230X
journals.iucr.org/f

Co-crystal structure of the *Fusobacterium ulcerans* ZTP riboswitch using an X-ray free-electron laser

Christopher Jones, Brandon Tran, Chelsie Conrad, Jason Stagno, Robert Trachman, Pontus Fischer, Alke Meents and Adrian Ferré-D'Amaré

Acta Cryst. (2019). F**75**, 496–500

STRUCTURAL BIOLOGY COMMUNICATIONS

ISSN 2053-230X

Co-crystal structure of the *Fusobacterium ulcerans* ZTP riboswitch using an X-ray free-electron laser

Christopher Jones,[a]‡ Brandon Tran,[a]‡ Chelsie Conrad,[b] Jason Stagno,[b] Robert Trachman III,[a] Pontus Fischer,[c,d] Alke Meents[c,d] and Adrian Ferré-D'Amaré[a]*

[a]Biochemistry and Biophysics Center, National Heart, Lung and Blood Institute, 50 South Drive, MSC 8012, Bethesda, MD 20892, USA, [b]Structural Biophysics Laboratory, Center for Cancer Research, National Cancer Institute, Frederick, Maryland, USA, [c]Center for Free Electron Laser Science, Deutsches Elektronen-Synchrotron, Notkestrasse 85, 22607 Hamburg, Germany, and [d]Photon Science, Deutsches Elektronen-Synchrotron, Notkestrasse 85, 22607 Hamburg, Germany. *Correspondence e-mail: adrian.ferre@nih.gov

Received 26 March 2019
Accepted 15 June 2019

Edited by K. K. Kim, Sungkyunkwan University School of Medicine, Republic of Korea

‡ These authors contributed equally to this work.

Keywords: RNA structure; riboswitches; ZTP; X-ray free-electron lasers.

PDB reference: *Fusobacterium ulcerans* ZTP riboswitch, 6od9

Supporting information: this article has supporting information at journals.iucr.org/f

Riboswitches are conformationally dynamic RNAs that regulate gene expression by binding specific small molecules. ZTP riboswitches bind the purine-biosynthetic intermediate 5-aminoimidazole-4-carboxamide riboside 5′-monophosphate (ZMP) and its triphosphorylated form (ZTP). Ligand binding to this riboswitch ultimately upregulates genes involved in folate and purine metabolism. Using an X-ray free-electron laser (XFEL), the room-temperature structure of the *Fusobacterium ulcerans* ZTP riboswitch bound to ZMP has now been determined at 4.1 Å resolution. This model, which was refined against a data set from ∼750 diffraction images (each from a single crystal), was found to be consistent with that previously obtained from data collected at 100 K using conventional synchrotron X-radiation. These experiments demonstrate the feasibility of time-resolved XFEL experiments to understand how the ZTP riboswitch accommodates cognate ligand binding.

1. Introduction

X-ray free-electron lasers (XFELs) produce extremely brilliant, coherent photons that are useful for investigating the structures of biological macromolecules (for a review, see Chapman, 2019). XFELs allow crystals that are found to be unsuitable for diffraction experiments for structure determination using traditional synchrotron radiation, owing to either their small size or their sensitivity to radiation damage, to be utilized. Moreover, small crystals are ideal for mix-and-inject serial femtosecond crystallography experiments examining the conformational changes induced by ligand binding (Stagno *et al.*, 2017), in which a mixture of crystals incubated for varying times with the ligand of interest are sprayed directly into the X-ray beam.

Riboswitches, ligand-binding RNAs that regulate gene expression, are systems that would benefit from study using XFELs (Stagno *et al.*, 2017). The structures of riboswitches are often solved in their ligand-bound states (for a review, see Jones & Ferré-D'Amaré, 2017), but the dynamics involved in ligand binding, and the concomitant conformational changes required for regulating gene expression, are more difficult to characterize. ZTP riboswitches regulate gene expression in bacteria (Kim *et al.*, 2015) by binding to ZMP (also known as AICAR) or its triphosphorylated form ZTP, which accumulates in cells under folate stress (Rohlman & Matthews, 1990; Bochner & Ames, 1982). ZMP and ZTP have been found to bind ZTP riboswitches with similar apparent dissociation constants (Kim *et al.*, 2015), so either compound could activate the riboswitch to upregulate the expression of a downstream

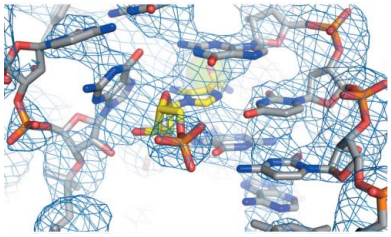

Table 1
Macromolecule-production information.

Source organism	*F. ulcerans*
Complete nucleic acid sequence of the construct produced	UAUCAGUUAUAUGACUGACGGAACGUGGAA UUAACCACAUGAAGUAUAACGAUGACAA UGCCGACCGUCUGGGCG

gene. These RNAs bind specifically to ZMP through hydrogen bonds and stacking interactions from nearby highly conserved residues (Jones & Ferré-D'Amaré, 2015). In addition, a magnesium ion coordinated to nearby phosphates (of residues U16 and C35) also directly coordinates to ZMP *via* a carbonyl O atom. It is unclear, however, whether the magnesium ion is coordinated prior to ZMP binding. Here, we have obtained a ZTP riboswitch structure from ∼750 microcrystals of the *Fusobacterium ulcerans* ZTP riboswitch bound to ZMP, a prerequisite for future serial crystallography experiments to understand the dynamics involved in formation of the ligand-binding pocket.

2. Materials and methods

2.1. Purification and crystallization

The 75-nucleotide *F. ulcerans* ZTP riboswitch (Table 1) was *in vitro* transcribed from a DNA template prepared by PCR from a plasmid as described previously (Jones & Ferré-D'Amaré, 2015). The template encodes the bacteriophage T7 RNA polymerase promoter, a self-cleaving hammerhead ribozyme and the ZTP riboswitch cDNA sequence. Prior to refolding, purified RNA was diluted in 50 m*M* HEPES–KOH pH 7.4, 150 m*M* KCl and a 1.25-fold excess of ZMP (Sigma–Aldrich), and refolded by heating at 80°C for 2 min and at 60°C for 2 min before adding 10 m*M* $MgCl_2$ and incubating on ice for at least 30 min. Crystals were grown by vapor diffusion in hanging drops consisting of 1.4 µl 100–200 µ*M* RNA in folding buffer and 0.7 µl of a reservoir solution comprising 28–32%(*w*/*v*) polyethylene glycol (PEG) 4000, 200 m*M* lithium sulfate, 100 m*M* bis-Tris–HCl pH 7 (Table 2). Drops were equilibrated over 0.5 ml reservoir solution at 21°C. Crystals generally appeared within two days.

2.2. Sample preparation and data collection

Before transferring the drops by pipetting, an equal volume of stabilizing solution consisting of the RNA folding buffer and reservoir solution supplemented with 15% glycerol was added to each drop. The mixture was pipetted repetitively to dislodge crystals from the substrate and precipitate, on which microcrystals tended to grow. The drops were combined and stored in a polypropylene microcentrifuge tube sandwiched between room-temperature cold packs en route to the beamline, where they were stored in a 21°C incubator until use. Upon arrival at the XFEL facility, visual inspection of the sample suggested that the crystals were intact.

Sample was prepared for data collection on a fixed-target Roadrunner goniometer as described previously (Roedig *et al.*, 2017). The Roadrunner chips were prepared from silicon wafers as described previously (Roedig *et al.*, 2015) and were washed with tetramethylammonium hydroxide and NH_4F/HF before use. The entire sample containing microcrystals was pipetted directly onto the center of a 31 000-pore silicon chip in a humidified chamber at room temperature. During sample application, the chip was wicked from the bottom with filter paper to draw crystals down into the pores, resulting in the sample covering approximately half of the chip surface. After ∼5 min, the chip was stationed in the Roadrunner goniometer and scanned at a rate of ∼120 images per second. Data were collected at 9516 eV on a Cornell–SLAC hybrid pixel-array detector (Table 3).

Table 2
Crystallization.

Method	Hanging-drop vapor diffusion
Plate type	15-well EasyXtal Tray (Qiagen)
Temperature (K)	293
RNA concentration (µ*M*)	100–200
Buffer composition of RNA solution	50 m*M* HEPES–KOH pH 7.4, 150 m*M* KCl, 10 m*M* $MgCl_2$, 1.25-fold excess of ZMP
Composition of reservoir solution	28–32% PEG 4000, 0.2 *M* $LiSO_4$, 0.1 *M* bis-Tris–HCl pH 7
Volume and ratio of drop	1.4 µl RNA solution + 0.7 µl reservoir solution
Volume of reservoir (ml)	0.5

Table 3
Data collection and processing.

Values in parentheses are for the highest resolution shell from a total of ten shells of refined data, truncated to 4.10 Å resolution.

Diffraction source	MFX, Linac Coherent Light Source
Wavelength (Å)	1.303
Temperature (K)	293
Detector	Cornell–SLAC pixel-array detector
Space group	$P3_221$
a, *b*, *c* (Å)	92.74, 92.74, 120.48
α, β, γ (°)	90, 90, 120
Resolution range (Å), collected	48.2–1.82
Resolution range (Å), refined	48.2–4.10 (4.25–4.10)
Total No. of reflections	53952 (5335)
No. of unique reflections	4979 (492)
Completeness (%)	99.1 (97.8)
Multiplicity	10.0 (7.1)
$\langle I/\sigma(I)\rangle$	3.5 (2.0)
R_{split}† (%)	76.2 (131.6)
$CC_{1/2}$	0.43 (0.16)

† R_{split} is defined by *CrystFEL* (White *et al.*, 2013) to be a figure of merit between two halves of a data set corrected by the loss in multiplicity.

2.3. Processing and refinement

Images containing diffraction patterns were identified using *Cheetah* (Barty *et al.*, 2014), yielding 1273 images with potential Bragg reflections. The data were indexed using *CrystFEL* (White *et al.*, 2013). Initial indexing without supplying unit-cell parameters resulted in ∼650 indexable images. Many of the indexed unit-cell parameters resembled the previously published unit-cell parameters for this RNA at 100 K (Jones & Ferré-D'Amaré, 2015), as well as solutions in Bravais lattices with lower symmetry (*e.g.* monoclinic). Indexing was repeated supplying the unit-cell parameters with several indexing methods (*XDS*, *mosflm-latt-cell*, *mosflm-nolatt-cell*, *dirax-nolatt-cell*) to improve the indexing hit rate to

Table 4
Structure refinement.

Resolution range (Å), refined	48.2–4.10 (4.25–4.10)
CC* cutoff	0.50
No. of reflections, working set	4771
No. of reflections, test set	208
Final R_{work}	0.258 (0.344)
Final R_{free}	0.308 (0.462)
No. of non-H atoms	
RNA	2651
Ion	9
Ligand	44
Water	6
Total	2710
R.m.s. deviations	
Bonds (Å)	0.001
Angles (°)	0.394
Average B factors (Å^2)	
RNA	84.2
Ion	62.9
Ligand	54.9
Water	49.2

762 indexable images. The resolution cutoff criterion was to include data from resolution shells with a CC* above 0.5 (*i.e.* $CC_{1/2} > \sim 0.15$; Karplus & Diederichs, 2015). The last shell to satisfy this criterion had a highest resolution of 4.1 Å.

2.4. Structure solution and refinement

Molecular replacement was performed with *Phaser* (McCoy *et al.*, 2007) using the previously determined *F. ulcerans* ZTP riboswitch model with all ions removed except for the magnesium ion that interacts with ZMP in the ligand-binding site (Jones & Ferré-D'Amaré, 2015). Simulated-annealing, energy and tightly restrained individual *B*-factor refinement was performed in *PHENIX* (Adams *et al.*, 2010) using a 4.1 Å resolution cutoff. Refinement at higher resolution cutoffs (*e.g.* 3.0–4.0 Å) resulted in poorer free *R* factors. The orientation of bound ZMP relied on previous structures. Additional rounds of refinement were interspersed with manual building in *Coot*. Figures were prepared using *PyMOL* (Schrödinger).

3. Results and discussion

During the course of optimizing the growth conditions for the preparation of large single crystals, microcrystals of the *F. ulcerans* ZTP riboswitch with dimensions of ~5–20 µm per side were grown and pooled for XFEL experiments [Fig. 1(*a*)]. In addition to diffraction data collection from microcrystals using an XFEL, the primary experimental difference between this data-collection strategy and previous strategies are the temperature (*i.e.* 293 and 100 K, respectively) and the potential hydration or dehydration that might occur during microcrystal sample application in the Roadrunner goniometer (Roedig *et al.*, 2017).

Although some crystals appeared to diffract to higher resolution [Fig. 1(*b*)], the nominal resolution of the data set is ~4.1 Å (Table 4), raising the possibility of obtaining a higher resolution in the future using a greater number of crystals. Using conventional synchrotron radiation at 100 K, crystals of the same RNA of ~0.3 mm per side diffracted to ~2.8 Å resolution with similar unit-cell parameters (Jones & Ferré-D'Amaré, 2015), so a substantial improvement in resolution could be achievable using a larger XFEL data set.

The refined structural model from the XFEL experiment was in general agreement with the previously determined cryocrystallographic structure (overall r.m.s.d. of 0.72 Å for all non-H atoms). Thus, at the current resolution limit, the changes in experimental conditions did not significantly alter the ZTP riboswitch structure. An exception is the appearance of a strong positive peak in the Fourier difference map near N7 of G25 in both RNA copies in the asymmetric unit [Fig. 2(*a*)]. Although the site would appear to be occupied by a cation, the placement of a potassium ion was insufficient to account for the feature. A cation was not observed in this site previously (Jones & Ferré-D'Amaré, 2015), although iridium hexammine ions occupied sites ~5 Å away (Jones & Ferré-D'Amaré, unpublished observations) when this ion was soaked in for *de novo* phasing. No larger cations are present in our crystallization conditions, raising the possibility of contamination during Roadrunner chip preparation. The only plausible cation in the buffers used to wash the Roadrunner

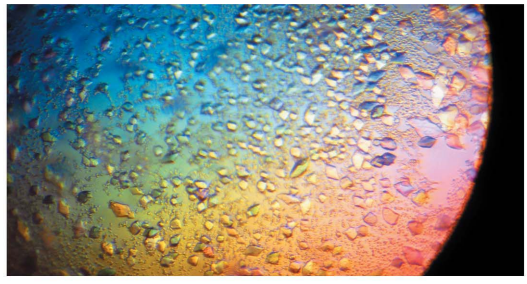

(*a*)

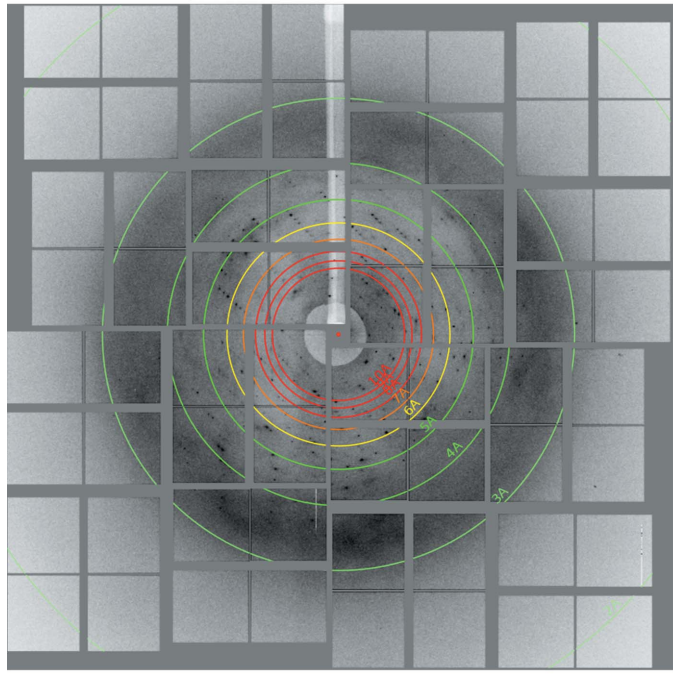

(*b*)

Figure 1
(*a*) Microcrystals of the ZTP riboswitch prior to harvesting for XFEL diffraction. (*b*) Still from XFEL data collection with diffraction extending beyond 3 Å resolution.

chips was tetramethylammonium, and refinement with this ion did not satisfy the residual features. As our crystallization solutions contained 0.2 *M* sulfate, one possible explanation is that sulfate anions occupy these sites, which would be unusual but not unprecedented (Edelmann *et al.*, 2017). While the placement of sulfate anions in each site satisfied the residual features [Fig. 2(*b*)], the refined *B* factors for the sulfates were much lower than for nearby RNA atoms. Although caesium was not known to be present in our crystals, Cs atoms have often been observed near guanine N7 positions (Liberman *et al.*, 2013; Pikovskaya *et al.*, 2011; Ren *et al.*, 2012), and we have recently used caesium to improve the crystallization of other RNAs, raising the possibility of cross-contamination. As the residual features were satisfied after refinement with caesium ions, the current model contains caesium in each position.

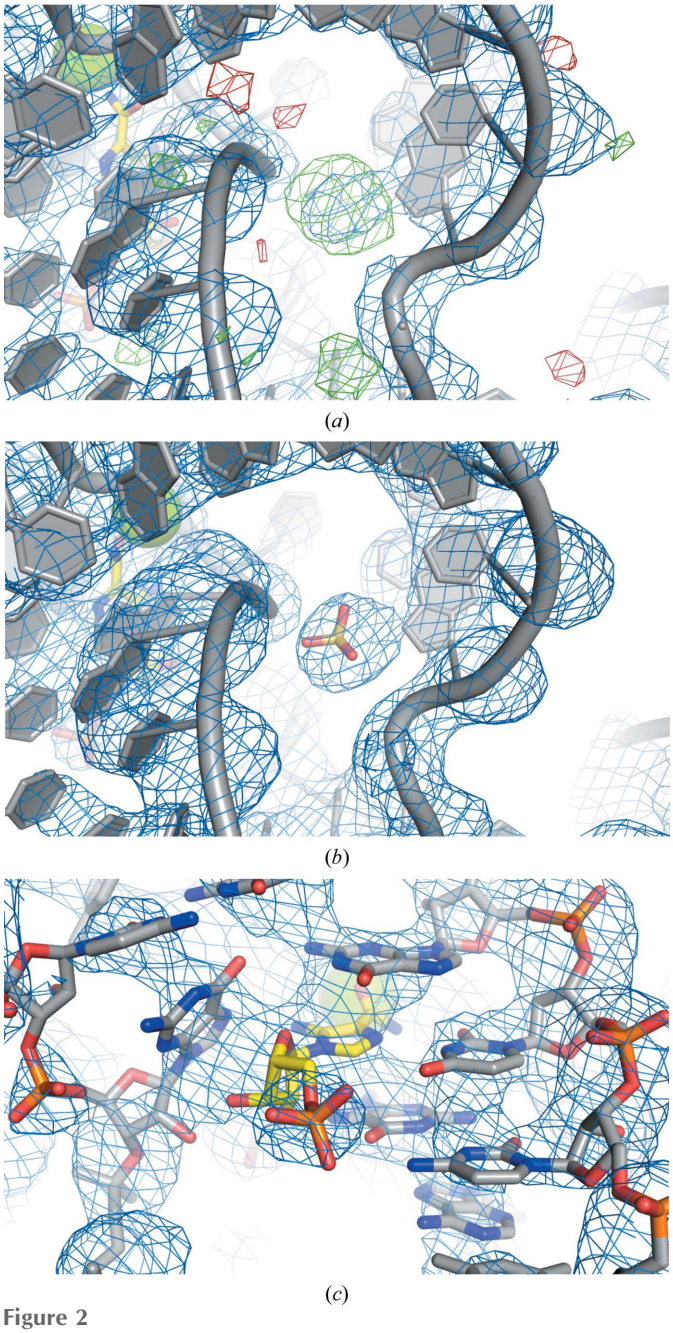

Figure 2
(*a*) Portions of electron-density maps prior to the placement of ions at G25, showing refined $2m|F_o| - D|F_c|$ maps (blue) and refined $m|F_o| - D|F_c|$ Fourier difference maps (green, positive) contoured at 1.5σ and 3σ, respectively, over the mean peak height. A cartoon model of the RNA is shown for clarity. The ligand-binding site is visible on the left side with bound ZMP (yellow) and magnesium ion (green sphere). (*b*) The same region after placement of the sulfate ion (sticks), showing the refined $2m|F_o| - D|F_c|$ map contoured at 1.5σ over the mean peak height. (*c*) Portions of the same map showing the ZMP-binding site.

Taken together, this work demonstrates the feasibility of examining the mechanism of ligand binding by the ZTP riboswitch using XFELs at room temperature. The ZTP riboswitch utilizes a highly conserved pseudoknot and bound magnesium ion to recognize its ligand [Fig. 2(*c*)], and is distinctly different from the adenine and guanine riboswitches both in overall architecture and in the mechanism of ligand recognition (Batey, 2012). Thus, future investigation of the ZTP riboswitch would test the previously proposed model for the function of the adenine riboswitch, in which a marginally stable helix responds to ligand binding to modulate the regulatory outcome (Stagno *et al.*, 2017; Jones & Ferré-D'Amaré, 2017). Moreover, it is unclear whether the bound Mg^{2+} ion occupies the pocket before or after ZMP binding and how other critical interactions reorient upon ligand binding to ultimately regulate gene expression.

Acknowledgements

We thank the staff at the Linac Coherent Light Source for XFEL support and Y.-X. Wang (National Cancer Institute) for graciously providing XFEL beam time.

Funding information

This work was supported in part by a career transition award from the National Heart, Lung and Blood Institute (NHLBI) to CPJ (K22HL139920), an NIH Director's Division of Intramural Research Innovation Award (to Y-XW and ARF) and the intramural programs of the National Cancer Institute and the NHLBI, NIH.

References

Adams, P. D., Afonine, P. V., Bunkóczi, G., Chen, V. B., Davis, I. W., Echols, N., Headd, J. J., Hung, L.-W., Kapral, G. J., Grosse-Kunstleve, R. W., McCoy, A. J., Moriarty, N. W., Oeffner, R., Read, R. J., Richardson, D. C., Richardson, J. S., Terwilliger, T. C. & Zwart, P. H. (2010). *Acta Cryst.* D**66**, 213–221.
Barty, A., Kirian, R. A., Maia, F. R. N. C., Hantke, M., Yoon, C. H., White, T. A. & Chapman, H. (2014). *J. Appl. Cryst.* **47**, 1118–1131.
Batey, R. T. (2012). *Q. Rev. Biophys.* **45**, 345–381.
Bochner, B. R. & Ames, B. N. (1982). *Cell*, **29**, 929–937.
Chapman, H. N. (2019). *Annu. Rev. Biochem.* **88**, 35–58.
Edelmann, F. T., Schlundt, A., Heym, R. G., Jenner, A., Niedner-Boblenz, A., Syed, M. I., Paillart, J. C., Stehle, R., Janowski, R., Sattler, M., Jansen, R. P. & Niessing, D. (2017). *Nature Struct. Mol. Biol.* **24**, 152–161.
Jones, C. P. & Ferré-D'Amaré, A. R. (2015). *Nature Struct. Mol. Biol.* **22**, 679–685.
Jones, C. P. & Ferré-D'Amaré, A. R. (2017). *Annu. Rev. Biophys.* **46**, 455–481.
Karplus, P. A. & Diederichs, K. (2015). *Curr. Opin. Struct. Biol.* **34**, 60–68.

Kim, P. B., Nelson, J. W. & Breaker, R. R. (2015). *Mol. Cell*, **57**, 317–328.
Liberman, J. A., Salim, M., Krucinska, J. & Wedekind, J. E. (2013). *Nature Chem. Biol.* **9**, 353–355.
McCoy, A. J., Grosse-Kunstleve, R. W., Adams, P. D., Winn, M. D., Storoni, L. C. & Read, R. J. (2007). *J. Appl. Cryst.* **40**, 658–674.
Pikovskaya, O., Polonskaia, A., Patel, D. J. & Serganov, A. (2011). *Nature Chem. Biol.* **7**, 748–755.
Ren, A., Rajashankar, K. R. & Patel, D. J. (2012). *Nature (London)*, **486**, 85–89.
Roedig, P., Ginn, H. M., Pakendorf, T., Sutton, G., Harlos, K., Walter, T. S., Meyer, J., Fischer, P., Duman, R., Vartiainen, I., Reime, B., Warmer, M., Brewster, A. S., Young, I. D., Michels-Clark, T., Sauter, N. K., Kotecha, A., Kelly, J., Rowlands, D. J., Sikorsky, M., Nelson, S., Damiani, D. S., Alonso-Mori, R., Ren, J., Fry, E. E., David, C., Stuart, D. I., Wagner, A. & Meents, A. (2017). *Nature Methods*, **14**, 805–810.
Roedig, P., Vartiainen, I., Duman, R., Panneerselvam, S., Stübe, N., Lorbeer, O., Warmer, M., Sutton, G., Stuart, D. I., Weckert, E., David, C., Wagner, A. & Meents, A. (2015). *Sci. Rep.* **5**, 10451.
Rohlman, C. E. & Matthews, R. G. (1990). *J. Bacteriol.* **172**, 7200–7210.
Stagno, J. R., Liu, Y., Bhandari, Y. R., Conrad, C. E., Panja, S., Swain, M., Fan, L., Nelson, G., Li, C., Wendel, D. R., White, T. A., Coe, J. D., Wiedorn, M. O., Knoska, J., Oberthuer, D., Tuckey, R. A., Yu, P., Dyba, M., Tarasov, S. G., Weierstall, U., Grant, T. D., Schwieters, C. D., Zhang, J., Ferré-D'Amaré, A. R., Fromme, P., Draper, D. E., Liang, M., Hunter, M. S., Boutet, S., Tan, K., Zuo, X., Ji, X., Barty, A., Zatsepin, N. A., Chapman, H. N., Spence, J. C. H., Woodson, S. A. & Wang, Y. (2017). *Nature (London)*, **541**, 242–246.
White, T. A., Barty, A., Stellato, F., Holton, J. M., Kirian, R. A., Zatsepin, N. A. & Chapman, H. N. (2013). *Acta Cryst.* D**69**, 1231–1240.